nature medicine

Cardiac BIN1 folds T-tubule membrane, controlling ion flux and limiting arrhythmia

TingTing Hong[1,8], Huanghe Yang[2,3,8], Shan-Shan Zhang[1], Hee Cheol Cho[1], Mariya Kalashnikova[1], Baiming Sun[1], Hao Zhang[4], Anamika Bhargava[5], Michael Grabe[4], Jeffrey Olgin[6], Julia Gorelik[5], Eduardo Marbán[1], Lily Y Jan[2–4,7] & Robin M Shaw[1]

Cardiomyocyte T tubules are important for regulating ion flux. Bridging integrator 1 (BIN1) is a T-tubule protein associated with calcium channel trafficking that is downregulated in failing hearts. Here we find that cardiac T tubules normally contain dense protective inner membrane folds that are formed by a cardiac isoform of BIN1. In mice with cardiac *Bin1* deletion, T-tubule folding is decreased, which does not change overall cardiomyocyte morphology but leads to free diffusion of local extracellular calcium and potassium ions, prolonging action-potential duration and increasing susceptibility to ventricular arrhythmias. We also found that T-tubule inner folds are rescued by expression of the BIN1 isoform BIN1+13+17, which promotes N-WASP–dependent actin polymerization to stabilize the T-tubule membrane at cardiac Z discs. BIN1+13+17 recruits actin to fold the T-tubule membrane, creating a 'fuzzy space' that protectively restricts ion flux. When the amount of the BIN1+13+17 isoform is decreased, as occurs in acquired cardiomyopathy, T-tubule morphology is altered, and arrhythmia can result.

Cardiac T tubules are highly branched invaginations of cardiomyocyte sarcolemma. T tubules are primarily transverse to the cardiomyocyte long axis and wrap around sarcomeric Z discs[1]. As an organelle involved in the initiation of calcium transients[2], the T-tubule system helps determine the strength of each heartbeat by concentrating L-type calcium channels (LTCCs) and positioning them in close proximity with ryanodine receptors at the sarcoplasmic reticulum[2–4]. The lumen of T tubules are continuous with the extracellular milieu, which is rich in calcium. During each heartbeat, an action potential triggers extracellular calcium entry into the cell through LTCCs, increasing the amount of local intracellular calcium, activating nearby ryanodine receptors and inducing a large calcium release from intracellular sarcoplasmic reticulum stores, resulting in cellular contraction. Thus, T tubules help regulate efficient beat-to-beat calcium flux.

There is growing evidence that extracellular and intracellular diffusion near the T-tubule sarcolemma is restricted, creating local regions of ion accumulation known as 'fuzzy space'[5–8]. Even though the overall diameter of T-tubule lumen is 20–450 nm[1], T tubules may be accessible only to ions and small nanoparticles (≤11 nm)[9]. T-tubule diffusion coefficients for extracellular ions are ~95 μm^2 per second for calcium ions[7] and ~85 μm^2 per second for potassium ions, which are five to ten times slower than their diffusion rates in bulk extracellular space[8]. At fast heart rates, rapid transmembrane flux and limited diffusion can result in depleted T-tubule lumen calcium[5,10] and elevation of T-tubule lumen potassium[8], affecting the driving force for transmembrane ion flux and decreasing action-potential duration[11].

Although T-tubule lumen is known to have connected branch points[1], this structural feature does not explain highly restricted diffusion. In failing hearts, T tubules are remodeled, resulting in fewer but larger T tubules[12–14]. In addition, in failing hearts action potentials are prolonged[15] and intracellular calcium overload occurs[16], which results in arrhythmias[16]. Action-potential duration and calcium handling are strongly influenced by T tubule–associated currents, but without a better understanding of T-tubule anatomy, it remains difficult to clarify the impact of T tubules on cardiac electrophysiology or determine the impact of altered T tubules on disease.

Recent studies have suggested that the membrane scaffolding protein BIN1 is a regulator of T-tubule structure and function. BIN1, a member of the BAR domain–containing protein superfamily, can induce LTCC-enriched membrane folds in cell lines and immature muscle cells[17,18]. In adult cardiomyocytes, BIN1 localizes to cardiac T tubules and facilitates cytoskeleton-based calcium channel trafficking to the T-tubule membrane[18]. The expression of BIN1 is transcriptionally decreased in acquired human and experimental animal heart failure, a condition that is also associated with both intracellular accumulation of LTCCs and abnormal T-tubule morphology[12,13,19,20]. A case of ventricular arrhythmia associated with BIN1 mutation has been reported[21].

[1]Cedars-Sinai Heart Institute, Cedars-Sinai Medical Center, Los Angeles, California, USA. [2]Department of Physiology, University of California San Francisco, San Francisco, California, USA. [3]Department of Biochemistry and Biophysics, University of California San Francisco, San Francisco, California, USA. [4]Cardiovascular Research Institute, University of California San Francisco, San Francisco, California, USA. [5]Imperial Center for Translational and Experimental Medicine, Imperial College, London, UK. [6]Division of Cardiology, Department of Medicine, University of California San Francisco, San Francisco, California, USA. [7]Howard Hughes Medical Institute, San Francisco, California, USA. [8]These authors contributed equally to this work. Correspondence should be addressed to R.M.S. (robin.shaw@cshs.org).

Received 18 February; accepted 24 March; published online 18 May 2014; doi:10.1038/nm.3543

In the present study, we studied the anatomy and function of cardiac T tubules in young adult mice with or without cardiac deletion of *Bin1*. With complementary *in vivo* and *ex vivo* studies, imaging, electrophysiology, biochemistry and mathematical modeling, we found that an alternatively spliced cardiac isoform of BIN1, BIN1+13+17, exists in the mouse heart, promotes N-WASP (also called WASL)-dependent actin polymerization and is responsible for generating actin-organized and densely packed T-tubule membrane folds. These folds create a physical diffusion barrier to extracellular ions and protect against arrhythmia. Our findings elucidate how cardiac T-tubule ionic concentrations can differ from the bulk extracellular ionic composition and why the T-tubule diffusion barrier disappears in heart failure, increasing the likelihood of ventricular arrhythmia.

RESULTS

The cardiomyocyte T-tubule membrane is densely folded by BIN1

Homozygous mice with global *Bin1* deletion suffer perinatal death due to cardiomyopathy[22]. To explore the role of BIN1 in cardiac T-tubule organization, we generated a cardiac-specific deletion of *Bin1* using α-myosin heavy chain (*Myh6*)-*cre*$^{+}$ (ref. 23) and *loxP*-flanked *Bin1* lines[24] to generate heterozygous (*Bin1* HT, *Bin1*$^{flox/+}$; *Myh6-cre*$^{+}$) and homozygous (*Bin1* HO, *Bin1*$^{flox/flox}$; *Myh6-cre*$^{+}$) mice. Use of *Myh6-cre* bypasses the embryonic lethality[25]. At 8–12 weeks, the overall body and heart phenotypes of wild-type (WT), *Bin1* HT (which have a reduction in BIN1 protein levels similar to that present in heart failure[19]) and *Bin1* HO animals were similar (**Supplementary Figs. 1** and **2**), consistent with the high cardiac reserve typical for young adult hearts[25]. We isolated adult cardiomyocytes from WT and *Bin1* HT animals and labeled them with a plasma membrane lipid dye, Di-8-ANNEPS, for live-cell imaging by spinning-disk confocal microscopy (**Fig. 1a–c** and **Supplementary Fig. 3**). We found that the distribution and regularity of T tubules were preserved in cardiomyocytes from *Bin1* HT hearts. However, T-tubule fluorescence was decreased in the *Bin1* HT cells, indicating less membrane along the T-tubule invaginations. We obtained similar results when we labeled membrane structures of freshly fixed cardiomyocytes with wheat germ agglutinin (WGA; **Supplementary Fig. 3b**). Electrophysiological measurement of cardiomyocyte T-tubule capacitance, which is 30% of the total cardiomyocyte capacitance[26], was decreased by 46% in *Bin1* HT cells (**Fig. 1d**), which had normal cell size (**Supplementary Fig. 3c**), confirming that cardiomyocytes deficient in BIN1 have a decreased amount of T-tubule membrane. The decrease in the amount of T-tubule membrane occurred despite preservation of the cellular content of T-tubule proteins (**Supplementary Fig. 4a**).

To visualize the impact of *Bin1* deletion on the T-tubule membrane *in situ*, we used transmission electron microscopy (TEM). We perfused

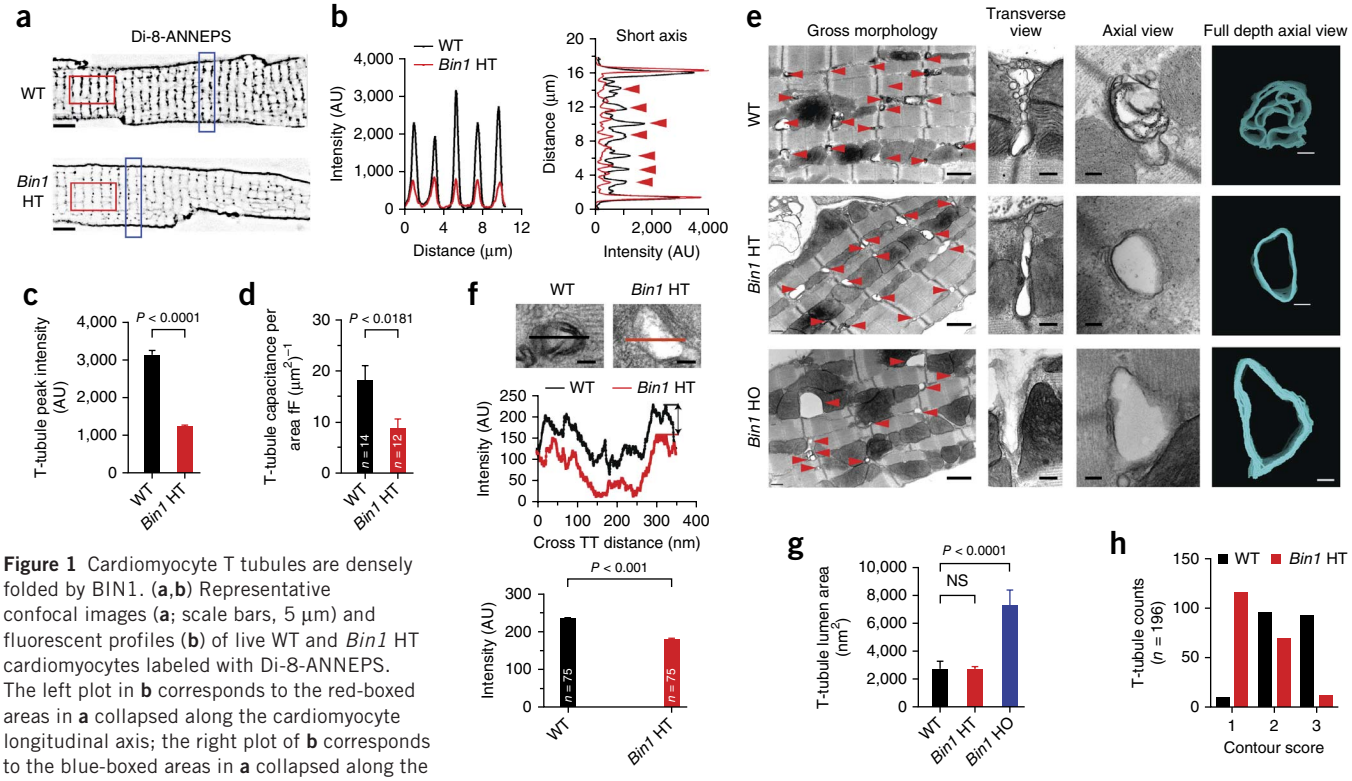

Figure 1 Cardiomyocyte T tubules are densely folded by BIN1. (**a**,**b**) Representative confocal images (**a**; scale bars, 5 μm) and fluorescent profiles (**b**) of live WT and *Bin1* HT cardiomyocytes labeled with Di-8-ANNEPS. The left plot in **b** corresponds to the red-boxed areas in **a** collapsed along the cardiomyocyte longitudinal axis; the right plot of **b** corresponds to the blue-boxed areas in **a** collapsed along the short axis. AU, arbitrary units. (**c**) Quantification of T-tubule peak intensity ($n = 40$ from 4–5 cells). (**d**) Cell size–normalized membrane capacitance in WT and *Bin1* HT cardiomyocytes (the *y*-axis zero point is the membrane capacitance of detubulated WT cardiomyocytes, which is 70% of whole-cell capacitance). (**e**) Two-dimensional TEM images (showing, left to right, gross morphology, transverse cross section and axial cross section) and three-dimensional electron tomography images (right) of WT and *Bin1* HT heart sections. Red arrowheads mark T-tubule cross sections. Scale bars (left to right), 1 μm; 250 nm; 100 nm; 100 nm. (**f**) Electron density profiles (middle) across individual T tubules (TT) marked by the red or black line in the images (top); average T-tubule electron density (bottom) ($n = 75$). The two-headed arrow marks the electron density difference between the WT and HT T-tubule membrane. (**g**) T-tubule lumen area of axial cross sections ($n = 80$). NS, not significant. (**h**) Cardiomyocyte T-tubule contour score (1, circular shape and no folds or spatial complexity; 2, noncircular shape and no folds or spatial complexity; 3, multiple folds with spatial complexity) distribution ($n = 196$, $P < 0.0001$ between WT and *Bin1* HT). All data are presented as the mean ± s.e.m. Cardiomyocytes are from three mice per genotype, and six left ventricular sections from two hearts per genotype were used for TEM analyses. Student's *t* test, one way-analysis of variance (ANOVA) and χ^2 test were used for statistical analyses.

freshly isolated whole mouse hearts with a calcium-containing fixative, sectioned the left ventricular free wall and post-fixed it with potassium ferricyanide, which enhances membrane contrast by forming calcium-dependent extracellular precipitates[27,28]. We found that the gross morphology of T-tubule invaginations was preserved in *Bin1* HT and HO cardiomyocytes (**Fig. 1e**). In high-magnification transverse and axial cross-sectional images of T tubules (**Fig. 1e** with quantification in **Fig. 1f**), we observed that, relative to WT T tubules, *Bin1* HT T tubules consistently had fewer calcium-dense membrane folds. As revealed by three-dimensional tomography (**Fig. 1e**), these membrane folds divide the WT T-tubule lumen into multiple spatial subdomains, which were lost in *Bin1* HT and *Bin1* HO T tubules. As a result, *Bin1* HT and *Bin1* HO T tubules contain one singular luminal space, which is enlarged in *Bin1* HO cardiomyocytes as compared to WT cardiomyocytes (quantification is shown in **Fig. 1g**). To numerically compare the extent to which the T tubules are contoured between WT and nondilated *Bin1* HT T tubules, we applied a T-tubule contour score to each axial cross-section image of the T tubule from multiple samples (three sections per heart and two hearts per genotype), assigning a score of 1 (round T-tubule lumen without folds and spatial complexity), 2 (noncircular contoured T-tubule lumen without folds and spatial complexity) or 3 (both round and noncircular T tubules with multiple folds and spatial complexity). We found that the T tubules in *Bin1* HT cardiomyocytes were markedly less contoured and folded (**Fig. 1h**). Consistent with these findings, T-tubule topology by scanning ion conductance microscopy revealed more distinct T-tubule openings with large diameters in *Bin1* HT cardiomyocytes as compared to WT cardiomyocytes, indicating that the BIN1-folded membrane creates a fuzzy space inside T tubules (**Supplementary Fig. 3d**).

BIN1 determines the T-tubule ion-diffusion barrier

What is the function of T-tubule membrane folds? One possibility, suggested by the TEM-identified calcium density at the T-tubule membrane (**Fig. 1f**), is that the folds create an extracellular microenvironment that is distinct from the bulk extracellular space. To test this possibility, we measured the dynamics of calcium ion diffusion into and out of T tubules by recording the calcium current, I_{Ca}, through LTCCs while rapidly changing the concentration of extracellular calcium. Baseline measurements revealed that, compared to WT cardiomyocytes, *Bin1* HT cardiomyocytes had a similar level of total Cav1.2 protein (also called CACNA1C) (**Supplementary Fig. 4a**), and, for membrane-inserted channels, a preserved preferential localization of LTCCs to T tubules. *Bin1* HT cardiomyocytes also had less total membrane LTCCs and less overall LTCC current than WT cardiomyocytes (**Supplementary Fig. 4b**), consistent with our previous report that BIN1 helps LTCC forward trafficking[18]. We next studied the activity of surface LTCCs by recording I_{Ca} decay kinetics after a rapid switch of extracellular perfusate from a physiological calcium conentration to zero calcium (buffered with 5 mM ethylene glycol tetraacetic acid (EGTA); **Fig. 2a**). After an initial delay, I_{Ca} decayed exponentially until all extracellular calcium inside the T tubules was removed or chelated (**Fig. 2b**). In *Bin1* HT cardiomyocytes, the length of the initial delay (X_0) was shortened by 64 ms compared to that of

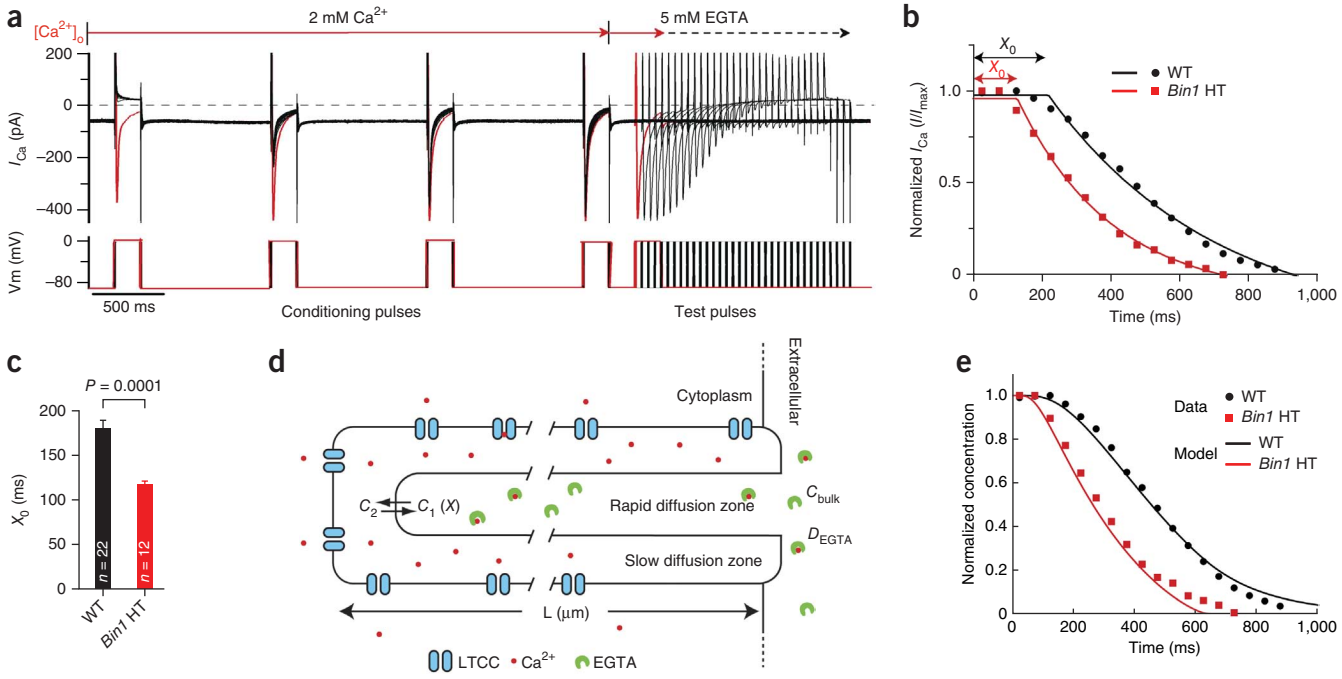

Figure 2 *Bin1* deletion increases extracellular Ca^{2+} diffusion. (**a**) A representative patch-clamp recording of LTCC-mediated I_{Ca} from a WT cardiomyocyte shifted from a 2 mM extracellular calcium solution to a calcium-free 5 mM EGTA solution. (**b**) Kinetics of I_{Ca} current changes using the protocol shown in **a**. The kinetics were fitted with one plateau followed by one phase of exponential decay. X_0 is the initial delay before I_{Ca} decays. (**c**) Comparison of X_0 for WT and *Bin1* HT cells. Data are presented as the mean ± s.e.m., and the *P* value was determined by Student's *t* test (WT ($n = 22$) and *Bin1* HT ($n = 12$) cardiomyocytes are from three mice for each genotype). (**d**) Diagram describing the salient features of a mathematical model for calcium diffusion (Online Methods). (**e**) Kinetics of I_{Ca} current decay computed using the model in **d** (model-derived values are indicated by the lines, and the recorded values are indicated by circles (WT) and squares (*Bin1* HT) from **b**). The normalized calcium concentration in the slow diffusion zone serves as a surrogate for the calcium current, as it is directly related to the inward Ca^{2+} driving force. In the model, WT T tubules contain a slow diffusion zone, consistent with the experimental data shown using WT cardiomyocytes. Removal of the slow diffusion barrier in **d** results in a shorter initial delay, as observed in the experimental data shown using *Bin1* HT cardiomyocytes.

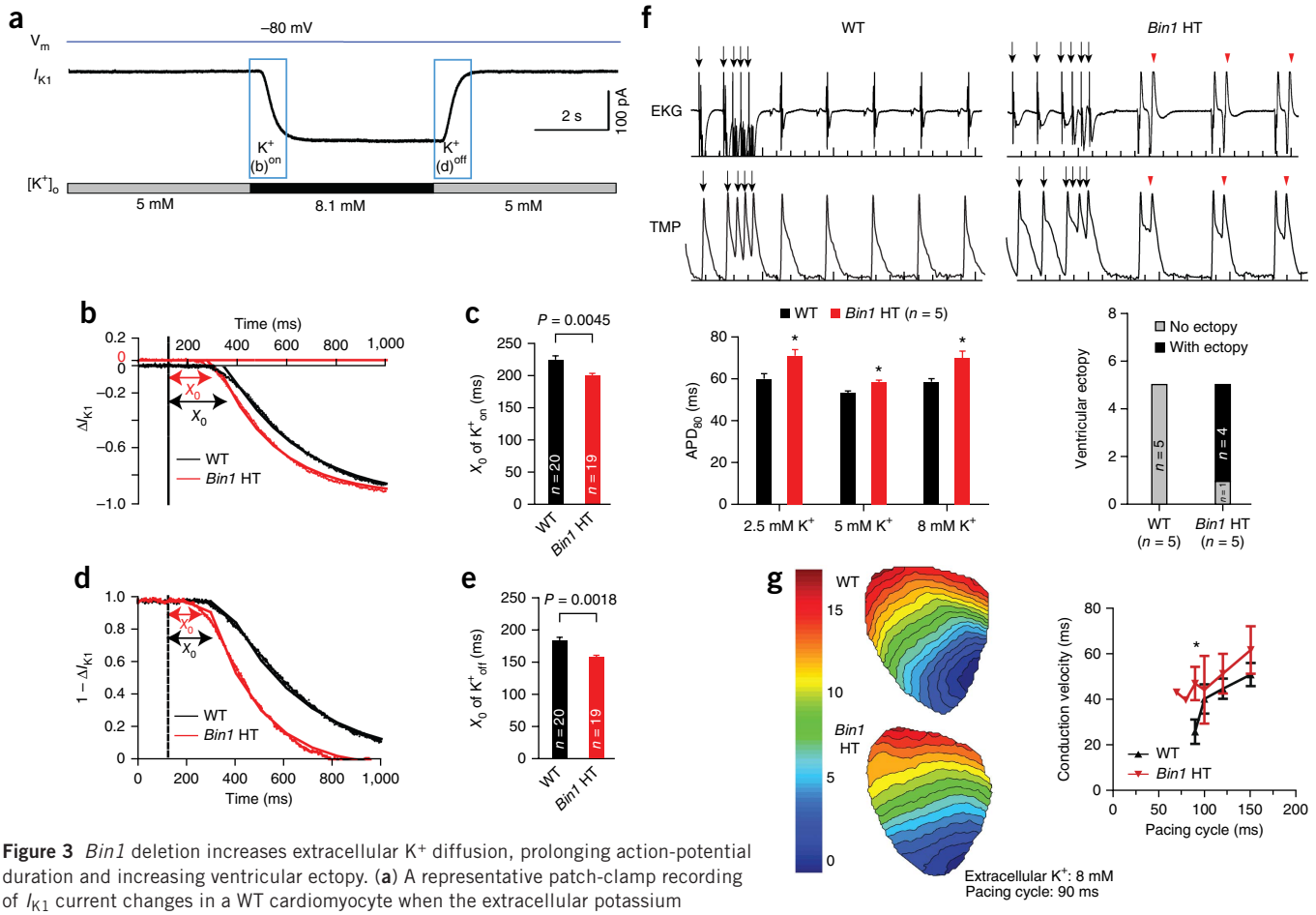

Figure 3 *Bin1* deletion increases extracellular K^+ diffusion, prolonging action-potential duration and increasing ventricular ectopy. (**a**) A representative patch-clamp recording of I_{K1} current changes in a WT cardiomyocyte when the extracellular potassium concentration is quickly switched. The labels (b) and (d) indicate that these portions of the plot are shown in more detail in panels **b** and **d**. (**b**) Kinetics of I_{K1} during K^+_{on} in WT and *Bin1* HT cardiomyocytes (dotted line, dead-volume time of 124 ms). (**c**) Comparison of the initial delay X_0 of K^+_{on} for WT ($n = 20$) and *Bin1* HT ($n = 19$) cardiomyocytes. (**d**) Kinetics of I_{K1} during K^+_{off} ($1 - \Delta I_{K1}$) in WT and *Bin1* HT cardiomyocytes. (**e**) Comparison of X_0 of K^+_{off} for WT ($n = 20$) and *Bin1* HT ($n = 19$) cardiomyocytes. (**f**) Top, representative tracings of EKG (first row) and transmembrane potential (TMP, second row) from isolated and Langendorff-perfused WT (left) and *Bin1* HT (right) hearts. Black arrows mark the pacing beats from the S1–S4 stimulation protocol, and red arrowheads mark ventricular ectopic beats. Bottom, action-potential duration (at 80% repolarization, APD_{80}) in *Bin1* HT hearts subjected to low (2.5 mM), normal (5 mM) or high (8 mM) potassium solution (left), and ventricular ectopy in *Bin1* HT hearts (right, incidence of arrhythmias during physiological buffer perfusion). (**g**) Ventricular activation map (left) and conduction velocity (right) of WT and *Bin1* HT hearts subjected to high potassium (8 mM) perfusion. $n = 4$–6. All data are presented as the mean ± s.e.m. In all the experiments, various n numbers of cardiomyocytes are obtained from three mice for each genotype. $^*P < 0.05$, Student's t test between the WT and *Bin1* HT groups.

WT cardiomyocytes (115 ± 5 (mean ± s.e.m.) ms compared to 179 ± 10 ms, $P = 0.0001$; **Fig. 2c**). To test whether the shortened X_0 could be due to increased ion diffusion within the T tubules, we implemented a simple mathematical model of calcium diffusion containing a slow diffusion zone (T-tubule folds; **Fig. 1e**,**h**), a rapid diffusion zone (T-tubule central lumen; tomography is shown in **Fig. 1e**) and EGTA chelation (**Fig. 2d**). The theoretical decay curve generated from the model superimposed with the experimental data in WT cardiomyocytes (**Fig. 2e**). Removal of the diffusion barrier resulted in a shortened X_0, as seen in *Bin1* HT cardiomyocytes (**Fig. 2e**). The autonomous mathematical algorithm that determined the best-fit T-tubule diffusion and anatomical parameters yielded values that were notably consistent with those previously measured (**Supplementary Table 1**), providing computational support for a model of BIN1-induced restricted extracellular calcium diffusion.

We next asked whether the physical barrier formed by BIN1-organized membrane folds applies to other ions. For potassium ions, which can also be affected by slow diffusion[8], we measured current from the inwardly rectifying potassium channel, I_{K1}, which maintains the cardiomyocyte resting membrane potential. We recorded the steady-state I_{K1} and its kinetics after rapid wash in and wash out of K^+ in T tubules (**Fig. 3a**). Similar to our observations of calcium diffusion, the decay of I_{K1} in response to an increase of extracellular potassium concentration from 5 to 8.1 mM (K^+_{on}) was significantly faster in *Bin1* HT compared to WT cardiomyocytes (**Fig. 3b**,**c**). Similarly, the response of I_{K1} to a decrease of extracellular potassium concentration from 8.1 mM to 5 mM (K^+_{off}) was significantly faster in *Bin1* HT cardiomyocytes compared to WT cardiomyocytes (**Fig. 3d**,**e**). The smaller difference in K^+ diffusion compared to calcium diffusion (24 ms compared to 64 ms) between WT and *Bin1* HT cells likely reflects less enrichment of I_{K1} compared to the LTCC in T tubules[29,30].

A change in extracellular diffusion will affect extracellular ion concentration, altering ion channel activity and electrophysiological parameters. We recorded electrocardiograms (EKGs) and performed whole-heart optical mapping on both WT and *Bin1* HT hearts. In *Bin1* HT hearts, action potentials were prolonged, and ectopy from

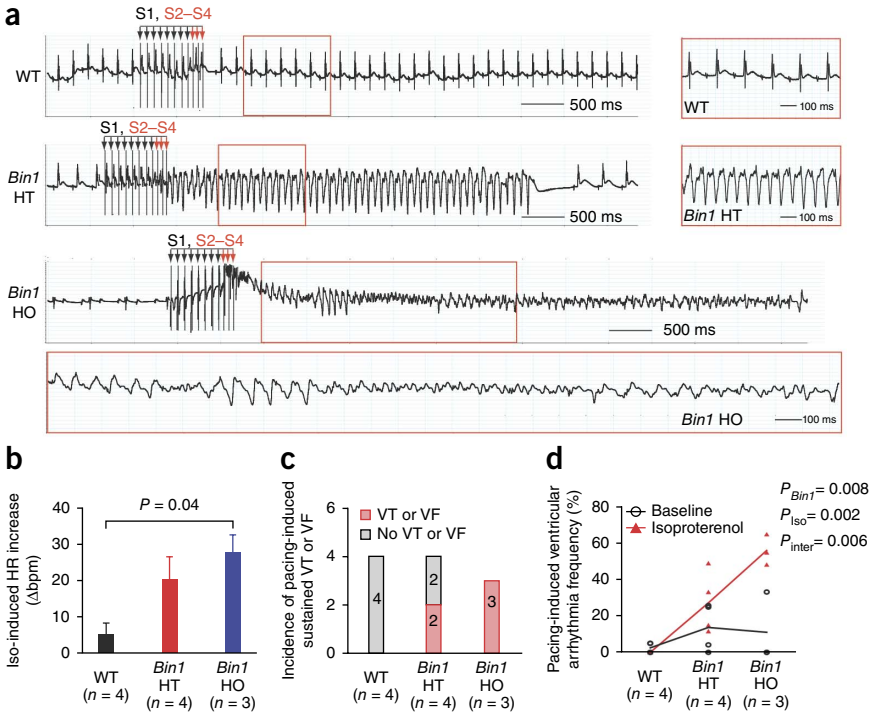

Figure 4 Ventricular arrhythmias induced by pacing and β adrenergic activation with isoproterenol. (**a**) Representative recordings of EKG after an S1–S4 stimulation protocol. Whereas normal sinus node beats resume immediately after pacing in WT mice (top), sustained monomorphic ventricular tachycardia (4.5 s) was induced in *Bin1* HT mice (middle), and sustained polymorphic VT alternating with VF (>20 s) was induced in *Bin1* HO mice (bottom). (**b**) Heart rate (HR) increase (change in beats per minute, Δbpm) in response to isoproterenol (Iso) in mice of the indicated genotypes (mean ± s.e.m., $P = 0.04$ by one-way ANOVA). (**c**) Incidence of sustained VT (>9 QRS) or VF in each group ($P = 0.03$ by χ^2 test when comparing WT and *Bin1* HO). (**d**) The frequency of ventricular arrhythmias before and after isoproterenol treatment in each group ($P < 0.01$ by two-way ANOVA, P_{Iso} compares before and after isoproterenol; P_{Bin1} compares the genotypes; and P_{inter} compares the effect of genotype on isoproterenol function).

afterdepolarizations occurred both spontaneously and with induction (**Fig. 3f**). If limited diffusion results in an increase in extracellular potassium in the local fuzzy space, then in theory, WT animals should be more sensitive to hyperkalemia-induced sodium channel block and conduction failure compared to *Bin1* HT animals[31]. When we perfused the hearts with a high-potassium solution, fast pacing induced a conduction block more readily in WT than in *Bin1* HT hearts (**Fig. 3g**). These data support a difference in extracellular potassium accumulation in WT and *Bin1* HT hearts.

Bin1 HT and HO mice exhibit inducible ventricular arrhythmias

Given the effects of BIN1 reduction on ion homeostasis and membrane-potential prolongation, we next studied *in vivo* arrhythmogenesis in WT, *Bin1* HT and *Bin1* HO mice subjected to ventricular pacing before and after intramyocardial injection of isoproterenol (**Fig. 4**). As is evident from representative EKG recordings (**Fig. 4a**), sinus rhythm resumed immediately after ectopic pacing in WT mice. However, sustained monomorphic ventricular tachycardia (VT) ensued after pacing in *Bin1* HT mice, and more severe sustained polymorphic VT alternating with ventricular fibrillation (VF) occurred in *Bin1* HO mice. The overall incidence of sustained VT (more than nine consecutive wide-complex beats)[32,33] or VF (**Fig. 4c**) as well as the frequency of pacing-induced arrhythmias (**Fig. 4d**) were significantly increased in *Bin1* HT and HO mice compared to WT mice. *Bin1* deletion also substantially increased the incidence of isoproterenol-induced arrhythmias (**Fig. 4d**), which have been linked to LTCC-mediated afterdepolarizations[34].

BIN1+13+17 uses F-actin to maintain T-tubule folds at Z discs

To identify the BIN1 isoform(s) responsible for T-tubule membrane folding, we explored cardiac splicing of *Bin1*, a gene that is encoded by 20 exons (**Fig. 5a**). Using PCR detection and sequencing of cloned fragments with primers flanking the alternatively spliced region between exons 10 (or 13) and 18 (**Fig. 5b**,**c**), we found that *Bin1* mRNA in adult mouse cardiomyocytes consists of several isoforms. The heart contains a small, constitutive version of *Bin1*, which does not contain exons 7, 11 or 13–17 (36% of all clones), as well as *Bin1+17* (including exon 17, 8%) and the alternatively spliced cardiac variants *Bin1+13* (48%) and *Bin1+13+17* (8%). Quantitative RT-PCR confirmed a similar expression pattern and further identified an increase in gene expression of all the *Bin1* variants in mature adult mouse cardiomyocytes relative to neonatal cardiomyocytes (**Fig. 5d**). Next, we used exon 13– or 17–specific BIN1 antibodies (**Fig. 5e**) to determine the distribution of BIN1 isoforms in adult mouse cardiomyocytes. Both antibodies to BIN1-13 and those to BIN1-17 localized to Z-line and/or T-tubule regions identified by anti–α-actinin and anti-Cav1.2 staining (**Fig. 5f**), indicating that BIN1+13+17 resides at T tubules.

The localization of BIN1+13+17 to T tubules implicates a role for this isoform in organizing membrane folds. When we expressed various BIN1 isoforms in *Bin1* HT cardiomyocytes, only BIN1+13+17 was capable of fully rescuing T-tubule membrane intensity (**Fig. 5g** and **Supplementary Fig. 5a**). Conversely, in WT adult mouse cardiomyocytes, *Bin1* knockdown using lentivirus-mediated shRNA targeting constitutive exon 2 or 13 decreased T-tubule membrane intensity in proportion to BIN1 protein reduction (**Supplementary Fig. 5b**).

To understand how BIN1+13+17 organizes the T-tubule membrane, we expressed GFP-tagged BIN1 isoforms in HeLa cells. Both confocal and TEM (**Fig. 6a–c**) imaging showed that only BIN1+13+17 induced the formation of elongated, F-actin–associated membrane folds (**Fig. 6d**), indicating a role of actin in BIN1+13+17–mediated fold formation. Cytochalasin D–induced stabilization of the barbed ends of F-actin at Z discs is known to help preserve the T-tubule structure of cultured cardiomyocytes[35]. We found that actin stabilization by cytochalasin D increased, whereas actin disruption by latrunculin A decreased, cardiac T-tubule membrane intensity (**Supplementary Fig. 6**). To further explore the differential roles of BIN1 isoforms in organizing actin, we studied their interactions with the actin polymerizing protein N-WASP, a known binding partner of the BAR domain protein amphiphysin 1 (ref. 36). Notably, although BIN1+13 did not bind to N-WASP (**Fig. 6e**), BIN1+13+17 did and could activate N-WASP to promote Arp2/3 nucleated actin polymerization (**Fig. 6f**). GST pulldown assays confirmed that BIN1+13+17 was associated with F-actin and α-actinin in adult

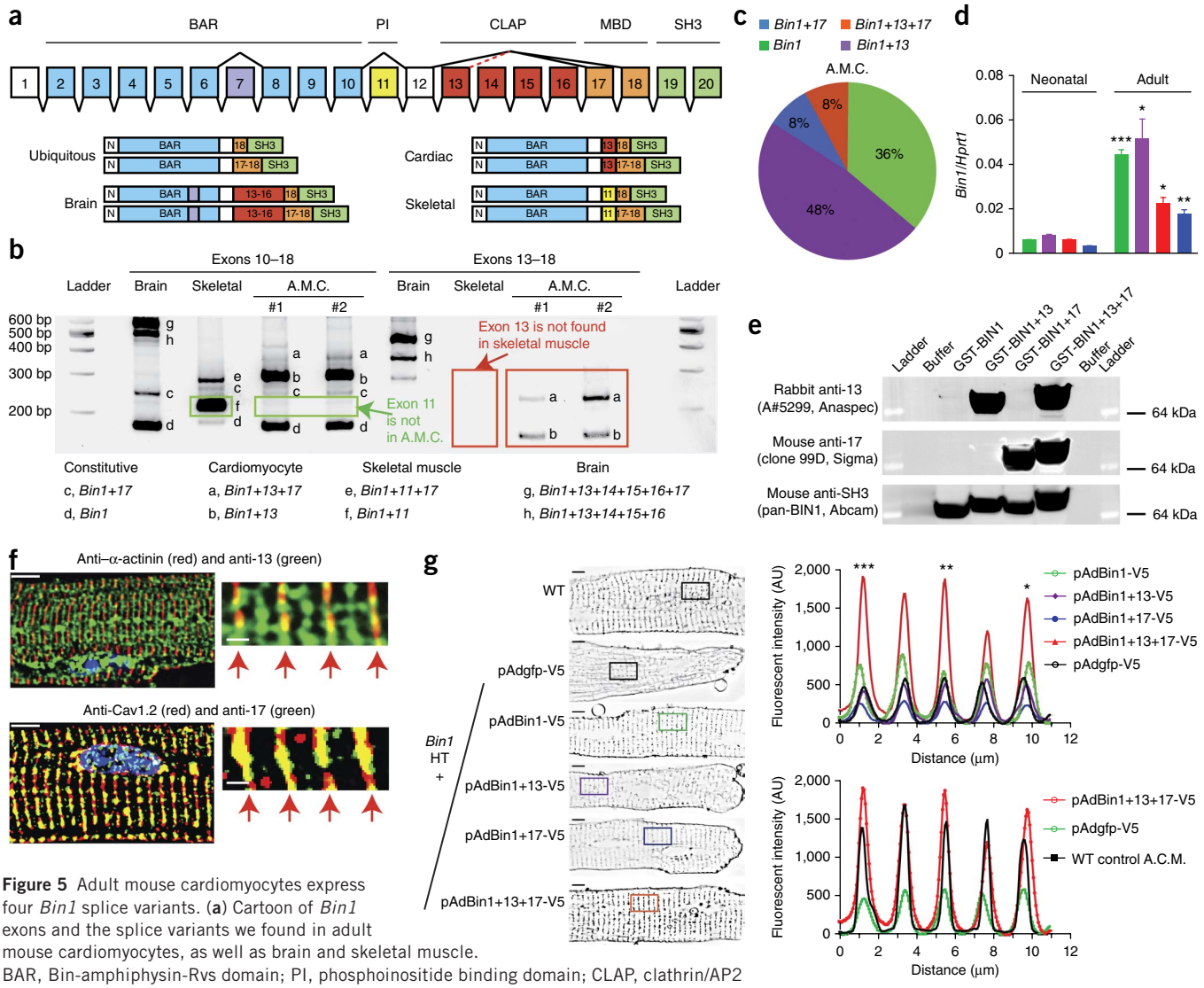

Figure 5 Adult mouse cardiomyocytes express four *Bin1* splice variants. (**a**) Cartoon of *Bin1* exons and the splice variants we found in adult mouse cardiomyocytes, as well as brain and skeletal muscle. BAR, Bin-amphiphysin-Rvs domain; PI, phosphoinositide binding domain; CLAP, clathrin/AP2 binding region; MBD, Myc-binding domain; SH3, SRC homology 3 domain. (**b**) Four *Bin1* splice variants with alternative inclusion of exons 13 and 17 were detected in adult mouse cardiomyocytes (A.M.C.) using PCR with primer sets flanking exons 10–18 or exons 13–18. PCR results in brain and skeletal muscle are also included. (**c**) The percentage of each *Bin1* splice variant represented in cDNA isolated from adult mouse cardiomyocytes after subcloning and sequencing using PCR primer sets flanking exons 10–18. (**d**) Quantitative RT-PCR analysis of each *Bin1* variant (*Bin1* normalized to the housekeeping gene *Hprt1* (*Bin1/Hprt1*)) in purified neonatal cardiomyocytes (postnatal day (P) 3, $n = 2$ litters with 8–10 pups each) or isolated adult mouse cardiomyocytes ($n = 5$ mice). (**e**) The specificity of antibodies to BIN1 exon 17 (anti-17, clone 99D, Sigma) and exon 13 (anti-13, A#5299, Anaspec) as assessed by western blot analysis. All four BIN1 isoforms are detected by pan-BIN1 antibody (rabbit anti–BIN1 SH3 domain). GST-tagged BIN1 isoforms are loaded as indicated. (**f**) Immunofluorescence labeling by the anti-13 and anti-17 antibodies in adult mouse cardiomyocytes (red arrows, Z line and TT region detected by α-actinin and Cav1.2 colabeling) Scale bars, 5 μm (left); 1 μm (right). (**g**) Representative confocal images (left; scale bars, 5 μm) and fluorescent profiles (right) of Di-8-ANNEPS membrane labeling in WT cardiomyocytes and in *Bin1* HT cardiomyocytes overexpressing GFP, BIN1, BIN1+13, BIN1+17 or BIN1+13+17 ($n = 5$ cells) transduced by adenovirus (pAd) carrying individual genes. All data are presented as the mean ± s.e.m. $^*P < 0.05$, $^{**}P < 0.01$, $^{***}P < 0.001$ by Student's *t* test (**c**) or two-way ANOVA followed by comparison between the GFP and BIN1+13+17 groups (**g**).

mouse hearts (**Fig. 6g**). These data indicate that BIN1+13+17 binds to and activates N-WASP to form elongated F-actin polymers for the development of membrane folds. By binding to α-actinin, BIN1+13+17 also connects these T-tubule membrane folds to Z discs, creating an ionic diffusion barrier within cardiac T tubules (**Fig. 6h**).

DISCUSSION

Here we report that cardiac T tubules are densely folded by a particular cardiac isoform of BIN1, resulting in a local extracellular microenvironment that resists diffusion with the bulk extracellular space and with important consequences for membrane electrophysiology. These results demonstrate a role for alternative splicing of BIN1 and its cytoskeleton-based membrane localization in folding the T-tubule membrane and regulating ion flux. In conditions where cardiac BIN1 expression is transcriptionally decreased, such as heart failure[19,20], loss of a T-tubule fuzzy space can increase arrhythmogenesis[16,37]. Our studies indicate that loss of BIN1 expression increases arrhythmogenesis independently of the organ-level structural changes that are associated with failing hearts.

Our results provide the first direct experimental evidence to our knowledge for the structural presence of a 'slow diffusion zone'

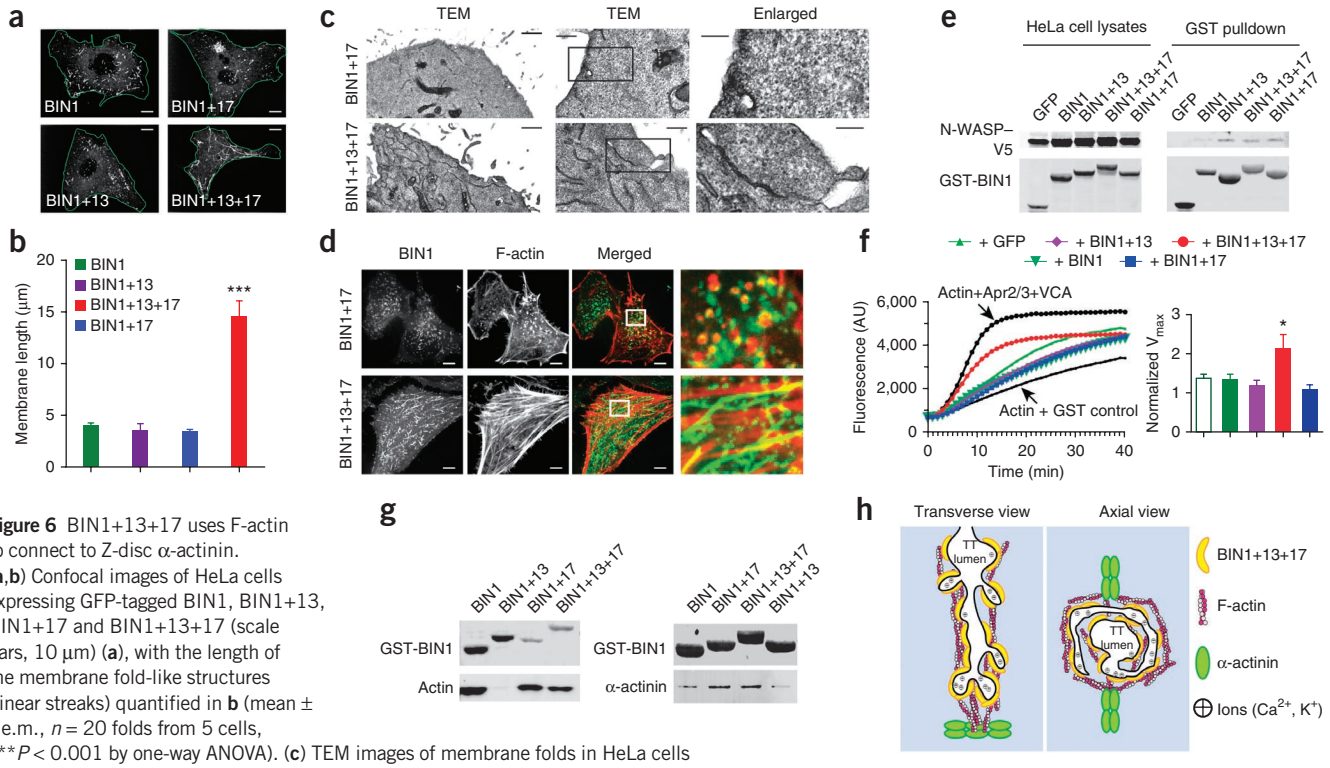

Figure 6 BIN1+13+17 uses F-actin to connect to Z-disc α-actinin. (**a**,**b**) Confocal images of HeLa cells expressing GFP-tagged BIN1, BIN1+13, BIN1+17 and BIN1+13+17 (scale bars, 10 μm) (**a**), with the length of the membrane fold-like structures (linear streaks) quantified in **b** (mean ± s.e.m., $n = 20$ folds from 5 cells, $^{***}P < 0.001$ by one-way ANOVA). (**c**) TEM images of membrane folds in HeLa cells transfected with BIN1+13+17 or BIN1+17. Scale bars, 1 μm (left); 0.5 μm (right two columns). (**d**) Live cell confocal images of HeLa cells expressing isoforms of GFP-BIN1 (green) and LifeAct-mCherry (red) (scale bars, 10 μm). The images on the right are zoomed-in images of the white-boxed areas in the merged images. (**e**) GST pulldown of GST-BIN1 isoforms and N-WASP–V5 in HeLa cells (representative blot of three experimental repeats). (**f**) *In vitro* pyrene-actin polymerization assay using purified Arp2/3, N-WASP and BIN1 isoforms. Left, a representative tracing of actin polymerization kinetics. Right, V_{max} data (normalized to actin alone) for polymerization kinetics (the bars from left to right are +GFP, +BIN1, +BIN1+13, +BIN1+13+17 and +BIN1+17). Data are presented as the mean ± s.e.m. ($n = 5$, $^{*}P < 0.05$ by one-way ANOVA). The negative control contains pyrene-actin alone with a GST control protein (GST-GFP, black line indicated by the bottom arrow), the positive control contains pyrene-actin supplemented with Arp2/3 and VCA (active domain of N-WASP, black line indicated by the top arrow), and the rest of the samples contain pyrene-actin supplemented with Arp2/3, N-WASP with GST-GFP or 1 μM of the GST-BIN1 isoform indicated. (**g**) Pulldowns of F-actin (left) and α-actinin (right) in adult heart lysates to which glutathione beads precoated with purified GST-BIN1 fusion protein were added (representative blot of three experimental repeats). (**h**) Schematic illustration of BIN1+13+17 forming an extracellular ionic diffusion barrier inside T tubules.

inside the T-tubule network, analogous to the 'fuzzy space' that has been previously proposed[6]. Future consideration of cardiomyocyte electrophysiology should take into account a separate slow diffusion zone at the inner face of T tubules that is organized by membrane folds. The slow diffusion zone and the T-tubule central lumen, separated by a resistive barrier, are predicted from computer models to change action-potential duration[11] and safeguard propagation of cardiac action potentials[38]. We found that removal of the BIN1-organized fuzzy space prolonged action-potential duration and increased ventricular arrhythmias. Removal of the ion diffusion barrier also significantly increased cardiac sensitivity to β adrenergic receptor activation. Thus, by creating a physical barrier that impedes the access of molecules such as catecholamine[9], folded T tubules serve as a protective mechanism to maintain cardiomyocyte homeostasis when the extracellular bulk environment fluctuates. It remains unclear how T-tubule folding affects efficient calcium-induced calcium release (CICR), as the T-tubule folds could in theory bring LTCCs closer to nearby ryanodine receptors. A recent study suggests that calcium-bound, activated LTCC undergoes a direct conformational change, a mechanism that, in addition to local Ca^{2+} diffusion, may facilitate cardiac CICR in a manner similar to the mechanisms known to underlie skeletal muscle CICR[39]. Future studies of intracellular ion diffusion, and the relationship between channel density and the T-tubule folds in *Bin1*-depleted cardiomyocytes, could enhance our understanding of calcium cycling.

Our study also describes cardiac-specific regulation of *Bin1* splicing. The exon 13–16–encoded clathrin binding domain targets neuronal BIN1 to clathrin-coated pits, facilitating endocytosis[40] and neurotransmitter reuptake[41]. Exon 11 encodes a phosphoinositide binding domain that targets skeletal BIN1 to the plasma membrane for skeletal tubular biogenesis[17]. We found that inclusion of exons 13 and 17 targets BIN1+13+17 to cardiac T tubules, resulting in extensive membrane folding. This cardiac isoform-dependent function of BIN1 involves N-WASP–mediated actin polymerization, helping BIN1+13+17 extend F-actin–organized membrane folds. Through α-actinin binding, BIN1+13+17 stabilizes these folds at cardiac Z discs. It may be that in addition to skeletal tubulogenesis[17], BIN1+11+17 has an analogous maintenance role in skeletal muscle[42], but given the marked differences in T-tubule number, size and location in skeletal compared to cardiac muscle, careful studies will be needed in each muscle subtype.

Other functions of the cardiac-spliced BIN1 isoforms unrelated to T-tubule folding are likely. Constitutive knockout of BIN1 causes embryonic cardiac hypertrophy and lethality[22], occurring before postnatal T-tubule development. We should note that in the cardiac-specific *Bin1* HO mice used in our study, which survive into adulthood, *Bin1* deletion was triggered by a promoter that activates only

in the perinatal stage, avoiding the non–T tubule related lethality. Furthermore, the most abundant cardiac isoform of BIN1 in mice is BIN1+13, which is known to be associated with cell proliferation[43]. Given that BIN1 has also been implicated in roles as varied as endocytosis and transcription[44,45], future studies will be helpful in defining the functional spectrum of different BIN1 isoforms in the heart.

In conclusion, we found that cardiac T tubules are densely folded by a particular BIN1 isoform, resulting in a retention of extracellular ions that modulates transmembrane ion flux and is thereby protective of heart function during stress. We previously found that BIN1 anchors microtubules to deliver LTCCs to the T-tubule membrane[18]. Our present findings indicate that BIN1 can also create T-tubule folds to which the channels can be delivered. When the amounts of BIN1 and other scaffolding proteins are reduced, such as in heart failure[14,19,46], not only are potential membrane anchor points lost but the membrane fold itself is no longer present. Loss of the folds can help explain the increase in ventricular arrhythmias that occurs in failing hearts[47].

METHODS

Methods and any associated references are available in the online version of the paper.

Note: Any Supplementary Information and Source Data files are available in the online version of the paper.

ACKNOWLEDGMENTS

This work was supported by US National Institutes of Health grants R01 HL094414 (R.M.S.), R37 MH065334 (L.Y.J.), WT090594 (J.G.), R21 GM100224 (M.G.), T32 HL116273 (S.-S.Z.) and K99/R00 HL109075 (T.H.) and by the American Heart Association (S.-S.Z. and R.M.S.). L.Y.J. is a Howard Hughes Medical Institute investigator. We thank E. Cingolani for helpful advice on designing the *in vivo* pacing protocol, D. Laury-Kleintop and G.C. Prendergast from the Lankenau Institute for Medical Research for *Bin1-loxP* mice, J. Mulholland and J.J. Perrino for TEM imaging at the Electron Microscopy Core of the Cell Sciences Imaging Facility at the Stanford University Medical Center, J. Smyth and R. Wirka for helpful discussions and T.S. Fong and T. Hitzeman for technical assistance.

AUTHOR CONTRIBUTIONS

All authors contributed to study design, analysis of the data and writing of the paper. T.H. was involved in the design and performance of all key experiments. H.Y. did the patch-clamp experiments. S.-S.Z. prepared mouse crossing, adenovirus and *Bin1* cloning experiments. H.C.C. and B.S. did the *in vivo* arrhythmia experiments. M.K. performed the actin polymerization assay. A.B. did the scanning ion-conductance microscopy imaging and analysis of T-tubule topology. H.Z. did the optical mapping studies. M.G. did the mathematical modeling.

COMPETING FINANCIAL INTERESTS

The authors declare no competing financial interests.

1. Soeller, C. & Cannell, M.B. Examination of the transverse tubular system in living cardiac rat myocytes by 2-photon microscopy and digital image-processing techniques. *Circ. Res.* **84**, 266–275 (1999).
2. Brette, F. & Orchard, C. T-tubule function in mammalian cardiac myocytes. *Circ. Res.* **92**, 1182–1192 (2003).
3. Cheng, H., Lederer, W.J. & Cannell, M.B. Calcium sparks: elementary events underlying excitation-contraction coupling in heart muscle. *Science* **262**, 740–744 (1993).
4. Bers, D.M. Cardiac excitation-contraction coupling. *Nature* **415**, 198–205 (2002).
5. Pásek, M., Simurda, J. & Christe, G. The functional role of cardiac T-tubules explored in a model of rat ventricular myocytes. *Philos. Trans. A. Math. Phys. Eng. Sci.* **364**, 1187–1206 (2006).
6. Lederer, W.J., Niggli, E. & Hadley, R.W. Sodium-calcium exchange in excitable cells: fuzzy space. *Science* **248**, 283 (1990).
7. Shepherd, N. & McDonough, H.B. Ionic diffusion in transverse tubules of cardiac ventricular myocytes. *Am. J. Physiol.* **275**, H852–H860 (1998).
8. Swift, F., Stromme, T.A., Amundsen, B., Sejersted, O.M. & Sjaastad, I. Slow diffusion of K^+ in the T tubules of rat cardiomyocytes. *J. Appl. Physiol.* **101**, 1170–1176 (2006).
9. Parfenov, A.S., Salnikov, V., Lederer, W.J. & Lukyanenko, V. Aqueous diffusion pathways as a part of the ventricular cell ultrastructure. *Biophys. J.* **90**, 1107–1119 (2006).
10. Pásek, M., Simurda, J. & Orchard, C.H. Role of T-tubules in the control of trans-sarcolemmal ion flux and intracellular Ca^{2+} in a model of the rat cardiac ventricular myocyte. *Eur. Biophys. J.* **41**, 491–503 (2012).
11. Pásek, M., Simurda, J., Orchard, C.H. & Christe, G. A model of the guinea-pig ventricular cardiac myocyte incorporating a transverse-axial tubular system. *Prog. Biophys. Mol. Biol.* **96**, 258–280 (2008).
12. Lyon, A.R. *et al.* Loss of T-tubules and other changes to surface topography in ventricular myocytes from failing human and rat heart. *Proc. Natl. Acad. Sci. USA* **106**, 6854–6859 (2009).
13. Wei, S. *et al.* T-tubule remodeling during transition from hypertrophy to heart failure. *Circ. Res.* **107**, 520–531 (2010).
14. Wagner, E. *et al.* Stimulated emission depletion live-cell super-resolution imaging shows proliferative remodeling of T-tubule membrane structures after myocardial infarction. *Circ. Res.* **111**, 402–414 (2012).
15. Aiba, T. & Tomaselli, G.F. Electrical remodeling in the failing heart. *Curr. Opin. Cardiol.* **25**, 29–36 (2010).
16. Sipido, K.R. Calcium overload, spontaneous calcium release, and ventricular arrhythmias. *Heart Rhythm* **3**, 977–979 (2006).
17. Lee, E. *et al.* Amphiphysin 2 (Bin1) and T-tubule biogenesis in muscle. *Science* **297**, 1193–1196 (2002).
18. Hong, T.T. *et al.* BIN1 localizes the L-type calcium channel to cardiac T-tubules. *PLoS Biol.* **8**, e1000312 (2010).
19. Hong, T.T. *et al.* BIN1 is reduced and Cav1.2 trafficking is impaired in human failing cardiomyocytes. *Heart Rhythm* **9**, 812–820 (2012).
20. Lyon, A.R. *et al.* Plasticity of surface structures and β_2-adrenergic receptor localization in failing ventricular cardiomyocytes during recovery from heart failure. *Circ Heart Fail* **5**, 357–365 (2012).
21. Böhm, J. *et al.* Case report of intrafamilial variability in autosomal recessive centronuclear myopathy associated to a novel BIN1 stop mutation. *Orphanet J. Rare Dis.* **5**, 35 (2010).
22. Muller, A.J. *et al.* Targeted disruption of the murine Bin1/Amphiphysin II gene does not disable endocytosis but results in embryonic cardiomyopathy with aberrant myofibril formation. *Mol. Cell. Biol.* **23**, 4295–4306 (2003).
23. Agah, R. *et al.* Gene recombination in postmitotic cells. Targeted expression of Cre recombinase provokes cardiac-restricted, site-specific rearrangement in adult ventricular muscle *in vivo*. *J. Clin. Invest.* **100**, 169–179 (1997).
24. Chang, M.Y. *et al. Bin1* ablation in mammary gland delays tissue remodeling and drives cancer progression. *Cancer Res.* **67**, 100–107 (2007).
25. Goonasekera, S.A. *et al.* Decreased cardiac L-type Ca^{2+} channel activity induces hypertrophy and heart failure in mice. *J. Clin. Invest.* **122**, 280–290 (2012).
26. Kawai, M., Hussain, M. & Orchard, C.H. Excitation-contraction coupling in rat ventricular myocytes after formamide-induced detubulation. *Am. J. Physiol.* **277**, H603–H609 (1999).
27. Hepler, P.K. Membranes in the mitotic apparatus of barley cells. *J. Cell Biol.* **86**, 490–499 (1980).
28. Franzini-Armstrong, C. Simultaneous maturation of transverse tubules and sarcoplasmic reticulum during muscle differentiation in the mouse. *Dev. Biol.* **146**, 353–363 (1991).
29. Komukai, K., Brette, F., Yamanushi, T.T. & Orchard, C.H. K^+ current distribution in rat sub-epicardial ventricular myocytes. *Pflugers Arch.* **444**, 532–538 (2002).
30. Pásek, M. *et al.* Quantification of T-tubule area and protein distribution in rat cardiac ventricular myocytes. *Prog. Biophys. Mol. Biol.* **96**, 244–257 (2008).
31. Shaw, R.M. & Rudy, Y. Electrophysiologic effects of acute myocardial ischemia. A mechanistic investigation of action potential conduction and conduction failure. *Circ. Res.* **80**, 124–138 (1997).
32. Mathur, N. *et al.* Sudden infant death syndrome in mice with an inherited mutation in RyR2. *Circ. Arrhythm. Electrophysiol.* **2**, 677–685 (2009).
33. Kannankeril, P.J. *et al.* Mice with the R176Q cardiac ryanodine receptor mutation exhibit catecholamine-induced ventricular tachycardia and cardiomyopathy. *Proc. Natl. Acad. Sci. USA* **103**, 12179–12184 (2006).
34. Marban, E., Robinson, S.W. & Wier, W.G. Mechanisms of arrhythmogenic delayed and early afterdepolarizations in ferret ventricular muscle. *J. Clin. Invest.* **78**, 1185–1192 (1986).
35. Tian, Q. *et al.* Functional and morphological preservation of adult ventricular myocytes in culture by sub-micromolar cytochalasin D supplement. *J. Mol. Cell. Cardiol.* **52**, 113–124 (2012).
36. Yamada, H. *et al.* Dynamic interaction of amphiphysin with N-WASP regulates actin assembly. *J. Biol. Chem.* **284**, 34244–34256 (2009).
37. Gaur, N., Rudy, Y. & Hool, L. Contributions of ion channel currents to ventricular action potential changes and induction of early afterdepolarizations during acute hypoxia. *Circ. Res.* **105**, 1196–1203 (2009).
38. Kim, J.M., Bursac, N. & Henriquez, C.S. A computer model of engineered cardiac monolayers. *Biophys. J.* **98**, 1762–1771 (2010).

39. Gez, L.S., Hagalili, Y., Shainberg, A. & Atlas, D. Voltage-driven Ca^{2+} binding at the L-type Ca^{2+} channel triggers cardiac excitation-contraction coupling prior to Ca^{2+} influx. *Biochemistry* **51**, 9658–9666 (2012).
40. Taylor, M.J., Perrais, D. & Merrifield, C.J. A high precision survey of the molecular dynamics of mammalian clathrin-mediated endocytosis. *PLoS Biol.* **9**, e1000604 (2011).
41. Butler, M.H. *et al.* Amphiphysin II (SH3P9; BIN1), a member of the amphiphysin/Rvs family, is concentrated in the cortical cytomatrix of axon initial segments and nodes of ranvier in brain and around T tubules in skeletal muscle. *J. Cell Biol.* **137**, 1355–1367 (1997).
42. Böhm, J. *et al.* Altered splicing of the BIN1 muscle-specific exon in humans and dogs with highly progressive centronuclear myopathy. *PLoS Genet.* **9**, e1003430 (2013).
43. Ge, K. *et al.* Mechanism for elimination of a tumor suppressor: aberrant splicing of a brain-specific exon causes loss of function of Bin1 in melanoma. *Proc. Natl. Acad. Sci. USA* **96**, 9689–9694 (1999).
44. Sakamuro, D., Elliott, K.J., Wechsler-Reya, R. & Prendergast, G.C. BIN1 is a novel MYC-interacting protein with features of a tumour suppressor. *Nat. Genet.* **14**, 69–77 (1996).
45. Elliott, K. *et al.* Bin1 functionally interacts with Myc and inhibits cell proliferation via multiple mechanisms. *Oncogene* **18**, 3564–3573 (1999).
46. Kashef, F. *et al.* Ankyrin-B protein in heart failure: identification of a new component of metazoan cardioprotection. *J. Biol. Chem.* **287**, 30268–30281 (2012).
47. Beuckelmann, D.J., Nabauer, M. & Erdmann, E. Alterations of K^+ currents in isolated human ventricular myocytes from patients with terminal heart failure. *Circ. Res.* **73**, 379–385 (1993).

ONLINE METHODS

Plasmids, antibodies and cell culture. Rabbit polyclonal antibody (A#5299, Anaspec) was raised against the BIN1 peptide LRKGPPVPPPP KHTPSKEMKQEQI (an epitope encoded by exon 13). We also used antibodies directed against the exon 17–encoded Myc-binding domain of BIN1 (99D, Sigma), pan-BIN1 rabbit antibody directed against the SH3 domain of BIN1 (Abcam), mouse and rabbit anti–α-actinin (Abcam), rabbit anti-Cav1.2 (Alomone), mouse and rabbit anti-V5 (Sigma), rabbit anti-actin (Sigma) and rabbit anti-GST (Santa Cruz Inc.). LifeAct-mCherry to identify actin in live cells was described previously[48]. Bovine N-WASP cDNA was obtained from Addgene (Plasmid 33019: Pcs2-Bnwasp). HeLa and FT293 cells (ATCC) were cultured in DMEM under standard mammalian cell conditions. Lipofectamine 2000 (Life Technologies) was used for cDNA transfections in HeLa cells.

Cloning. Total RNA was extracted from isolated mouse cardiomyocytes and reverse transcribed into cDNA using the iScript cDNA synthesis kit (Bio-Rad). The resulting *Bin1* cDNA was used for PCR amplification of the middle section, including the alternatively spliced region, using the following two primer sets: for exons 10–18, TTCACAGTCAAGGCCCAACC (forward) and ACCACCACAGCCGGAAGAGA (reverse); and for exons 13–18, TCCCCAAGTCCCCATCTCA (forward) and ACCACAGCCGGAAGAGAGCT (reverse). The primers also contained attB1/attB2 flanking sites. The cDNAs generated were then cloned using Gateway BP into pDONR/Zeo (Life Technology). A total of 100 entry clones of the cardiac *Bin1* middle section (exons 10–18, n = 100) were sequenced to identify a total of four distinct isoforms expressed in cardiomyocytes. The percentage of clones isolated for each variant was analyzed, and the data are presented in **Figure 5c**.

The same cloning approach was used to make full-length *Bin1* expression clones using primers ATGGCAGAGATGGGGAGCA (forward) and TCAC TGCACCCGCTCTGTAAA (reverse). The entry clones were sequenced to obtain clones representing all four cardiac BIN1 isoforms. The clones were then inserted into the vectors pDest-eGFP-N1 (Shaw Lab, available at Addgene), pDest-mCherry-N1 (Shaw Lab, available at Addgene), pcDNA3.2-V5-Dest (Life Technologies), pDest27-N-GST (Life Technologies) and pAdeno-V5-Dest (Life Technologies) by Gateway LR cloning to generate the final tagged expression clones and an adenovirus construct.

Quantitative RT-PCR analysis of cardiac *Bin1* variants in isolated adult and neonatal mouse cardiomyocytes. Adult mouse cardiomyocytes were isolated from 8-week-old C57BL/6 mouse hearts according to a previously established method[49]. Stepwise calcium reintroduction and slow centrifugation (40*g*) followed by plating on laminin-precoated dishes were used to generate a population of adult mouse cardiomyocytes, 90% of which were viable rod-shaped cells[49]. After neonatal (P3) cardiomyocyte isolation[18], we adopted an efficient nongenetic mitochondrial labeling approach using flow cytometry[50] (using BD Biosciences LSRII and FACSAriaII instruments) to separate cardiomyocytes with the highest mitochondrial dye intensity. The identity of the cells as cardiomyocytes was further confirmed by cardiac marker (Tnni3 and MF20) expression. Total RNA was then isolated from purified adult and neonatal cardiomyocytes using a Picopure RNA extraction kit (Arcturus), and cDNA was synthesized using the BioRad iScript kit. To determine the mRNA expression level of cardiac *Bin1* variants, we designed exon junction–specific primers to quantify splice variant levels by quantitative RT-PCR (qRT-PCR) in both P3 neonatal and adult mouse cardiomyocytes. Custom TaqMan exon-specific primers were generated to span the exon junctions of interest (12 and 13, 17 and 18, 12 and 17, 12 and 18) using the Custom TaqMan Assay Design Tool to ensure specificity and avoid repeats or SNPs. Assay A used the exon 12 and 13 junction to detect *Bin1+13* and *Bin1+13+17*; assay B used the exon 17 and 18 junction to detect both *Bin1+17* and *Bin1+13+17*; assay C used the exon 12 and 17 junction to detect only *Bin1+17*; and assay D used the exon 12 and 18 junction to detect only the smallest *Bin1* variant. The expression level of *Bin1+13+17* is derived by assay B – assay C, and the expression level of *Bin1+13* is estimated by assay A – (assay B – assay C). The custom probe sequences are: *Bin1_12_13*: TGACAA TGCCCCTGAGAAAGGGAACAAGAGCCCGTCACCTCCTCCAGATGGCT CCCCTGCTGCTACCCCTGAGATCAGAGTGAACCATGAGCCAGAGCCG GCCAGTGGGGCCTCACCCGGGGCTACCATCCCCAAGTCCCCATCTCA GCTCCGGAAAGGCCCACCTGTCCCTCCGCCTCCCAAACACACCCCAT CCAAGGAGATGAAGCAGGAGCAGATTCTCAGCCTTTTTGATGACGCA TTTGTCCCTGAGATCAGCGTGACCACCCCCTCCCAG 94 = ex11, 204 = ex12; *Bin1_12_17*: TGACAATGCCCCTGAGAAAGGGAACAAGAGCCCGT CACCTCCTCCAGATGGCTCCCCTGCTGCTACCCCTGAGATCAGAGTG AACCATGAGCCAGAGCCGGCCAGTGGGGCCTCACCCGGGGCTACCAT CCCCAAGTCCCCATCTCAGCCAGCAGAGGCCTCCGAGGTGGTGGGTG GAGCCCAGGAGCCAGGGGAGACAGCAGCCAGTGAAGCAACCTCC 94 = ex11,190 = ex16; *Bin1_17_18*: CCAGCAGAGGCCTCCGAGGTGGTGGGT GGAGCCCAGGAGCCAGGGGAGACAGCAGCCAGTGAAGCAACCTCCA GCTCTCTTCCGGCTGTGGTGGTGGAGACCTTCTCCGCAACTGTGAAT GGGGCGGTGGAGGGCAGCGCTGGGACTGGACGCTTGGACCTGCCCC CGGGATTCATGTTCAAG 31 = ex16, 141 = ex17; and *Bin1_12_18*: TGACAA TGCCCCTGAGAAAGGGAACAAGAGCCCGTCACCTCCTCCAGATGGCT CCCCTGCTGCTACCCCTGAGATCAGAGTGAACCATGAGCCAGAGCCG GCCAGTGGGGCCTCACCCGGGGCTACCATCCCCAAGTCCCCATCTCA GAGCTCTCTTCCGGCTGTGGTGGTGGAGACCTTCTCCGCAACTGTGA ATGGGGCGGTGGAGGGCAGCGCTGGGACTGGACGCTTGGACCTGCC CCCGGGATTCATGTTCAAG 94 = ex11,203 = ex17.

Generation of cardiac-specific *Bin1* heterozygote mice and cardiomyocyte isolation. All mouse procedures were reviewed and approved by the University of California and Cedars-Sinai Medical Center Institutional Animal Care and Use Committee. Heterozygote *Bin1*$^{flox/flox}$ mice[24] (with *loxP* sites flanking exon 3 of the *Bin1* gene) were interbred with *Myh6-cre* mice[23] to generate cardiomyocyte-specific *Bin1* heterozygous (*Bin1* HT, *Bin1*$^{flox/+}$; *Myh6-cre*$^{+}$) and homozygous (*Bin1* HO, *Bin1*$^{flox/flox}$; *Myh6-cre*$^{+}$) mice (detailed breeding strategies are listed in **Supplementary Fig. 1**). There were no phenotypic differences between mice of the other genotypes in the same litters (*Bin1*$^{+/+}$; *cre*$^{-}$, *Bin1*$^{+/+}$; *cre*$^{+}$, *Bin1*$^{flox/+}$; *cre*$^{-}$ and *Bin1*$^{flox/flox}$; *cre*$^{-}$). Hence, data from these mice are pooled as the WT group. Genotypes were confirmed by PCR, which was used to differentiate *Bin1*$^{+}$, *Bin1*^{flox} and *cre*$^{+}$ alleles. To confirm the efficiency of Cre-mediated deletion of *Bin1*, quantitative real-time PCR using TaqMan primer/probe sets (5′FAM/3′BHQ; Applied Biosystems) spanning the constitutively expressed exons 2 and 3 (Mm01158690_mH) were used to measure total transcription of the *Bin1* gene in cardiomyocyte cDNA from WT and *Bin1* HT mice. Similarly, transcription of the housekeeping gene *Hrpt1* and a cardiac-specific gene, *TnI3*, were measured using TaqMan primer/probe sets (Applied Biosystems). Quantitative real-time PCR reactions (10 µl) were performed in a 384-well format on an ABI 7900HT (Applied Biosystems).

Ventricular myocytes were isolated from 8- to 12-week-old WT and *Bin1* HT littermates after dissociation with collagenase II (2 mg ml^{-1}; Worthington) using a previously described method[49]. Each cellular experiment represents cardiomyocytes isolated from three sex-matched mice per genotype.

Adenoviral and lentiviral infection of adult mouse cardiomyocytes. For rescue experiments, *Bin1* HT cardiomyocytes were plated and infected 2 h later with GFP or a BIN1 isoform-overexpressing adenovirus (multiplicity of infection (MOI) 1,000) overnight, followed either by live-cell membrane imaging with Di-8-ANNEPS (Life Technologies) or by fixed-cell membrane imaging with Alexa 647–conjugated WGA (Life Technologies) after fixation with 4% paraformaldehyde (PFA). For *Bin1* knockdown experiments, cardiomyocytes were infected (MOI 5) overnight with lentiviruses (Sigma) expressing constitutive exon 2–targeting BIN1 shRNA (5′-CCGGAGACGAAGGACGAGCAGTTTG CTCGAGCAAACTGCTCGTCCTTCGTCTTTTTTG-3′) or exon 13–targeting BIN1 shRNA (5′-CCGGTGACGCATTTGTCCCTGAGATCTCGAGATCTGC AGGGACAAATGCGTCATTTTTG-3′). After viral infection, cardiomyocytes were cultured for 3 d before fixation for WGA-labeled membrane intensity analyses. For actin studies, freshly isolated cardiomyocytes were plated for 2 h and treated with 1 µM latrunculin A or 10 µM cytochalasin D overnight, followed by PFA fixation and T-tubule labeling with Alexa 647–conjugated WGA[51].

Membrane fluorescence labeling, immunofluorescence and imaging. Freshly isolated ventricular cardiomyocytes from both WT and *Bin1* HT mice were incubated with 10 µM Di-8-ANNEPS for 20 min at room temperature. The cells were then washed with HBSS to remove the remaining dye and imaged

with a spinning-disc confocal microscope. Di-8-ANEPPS–labeled cells were excited with a 488-nm laser, and emitted fluorescence was collected through a 580-nm emission filter. For conjugated WGA-labeled membrane fluorescence, freshly isolated cardiomyocytes were fixed with 4% PFA at room temperature for 30 min and labeled with Alexa 647–conjugated WGA at 4 °C overnight, followed by mounting in ProLong gold and imaging using a spinning-disc confocal microscope.

For all immunofluorescence experiments, cells were fixed in methanol at −20 °C for 5 min. After fixation, cardiomyocytes were permeablized and blocked with 0.5% Triton X-100 and 5% normal goat serum (NGS) in PBS for 1 h at room temperature. The cells were incubated with mouse antibody to BIN1 exon 17 (99D, 1:50, Sigma) and rabbit antibody to Cav1.2 (1:50, Alomone, ACC003) or rabbit antibody to BIN1 exon 13 (1:50, Anaspec) and mouse antibody to α-actinin (1:500, Abcam) overnight at 4 °C. After adenoviral infection, expression of the tagged protein was confirmed by anti-V5 (mouse anti-V5, Sigma, 1:500) labeling. Following incubation with primary antibodies and several washes with PBS, cells were incubated with goat anti-mouse IgG conjugated to Alexa Fluor 488 and goat anti-rabbit IgG (Life Technologies) conjugated to Alexa Fluor 555. Cells were then fixed and mounted with DAPI containing ProLong gold.

All imaging was performed on a Nikon Eclipse T*i* microscope with a 100× 1.49 numerical aperture (NA) or 60× 1.1 NA total internal reflection fluorescence (TIRF) objective and NIS Elements software. For BIN1 localization, isolated mouse cardiomyocytes were imaged at *z*-depth increments of 0.5 μm. Deconvolution of images was performed using Autoquant software (Media Cybernetics). High-resolution cardiomyocyte images were obtained using a spinning-disc confocal unit (Yokogawa CSU10) with diode-pumped solid state (DPSS) lasers (486, 561) generated from laser merge module 5 (Spectral applied research, CA) and captured by a high-resolution Cool SNAP HQ2 camera (Photometrics).

For live-cell imaging of BIN1-GFP and LifeAct-mCherry, HeLa cells were transfected with BIN1+17-GFP or BIN1+13+17-GFP, along with co-transfection of LifeAct-mCherry. Co-transfected cells were imaged in regular HBSS (Gibco) using a 100× 1.49 NA TIRF objective with spinning-disc confocal microscopy. Live images were captured using a high-resolution Cool SNAP HQ2 camera (Photometrics).

Topography scans were obtained from freshly isolated adult cardiomyocytes using scanning ion conductance microscopy as described previously[52].

Electron microscopy. For TEM study of the *in situ* ventricular cardiomyocyte membrane ultrastructure, whole mouse hearts were perfused with fixative (2% PFA and 2.5% glutaraldehyde in 0.1 M sodium cacodylate buffer and 50 mM $CaCl_2$, pH 7.4) at 3 ml per min at room temperature for 15 min before being stored at 4 °C in fixative. T tubules were labeled according to a previously established method[28]. Briefly, ultra-thin heart tissue sections were cut by a Leica Ultracut S microtome and post-fixed in OsO_4 (2% OsO_4 + 0.8% $K_3Fe(CN)_6$ in 0.1 M cacodylate buffer (pH 7.4) (Sigma)), followed by uranyl acetate (EM Science) incubation before being dehydrated in ethanol and embedded in epon resin. Tissue sections were imaged at 3,000×, 8,000× and 150,000× magnification using a transmission electron microscope (JEOL TEM1230 from the Electron Microscopy Core (EMC) of the Cell Sciences Imaging Facility (CSIF) at the Stanford University Medical Center). IMOD was used for three-dimensional reconstruction of TEM serial sections, and a two-axis tomography of T tubules was generated according to a previously established method[53,54].

Cardiomyocyte electrophysiology. Membrane capacitance and macroscopic calcium (I_{Ca}) and inward rectifying potassium channel–mediated I_{K1} currents were recorded by whole-cell voltage clamp of acutely isolated adult mouse cardiomyocytes. Patches were formed with borosilicate pipettes of 3–5 MΩ resistance. Data were acquired using an Axopatch 200-B patch-clamp amplifier and pClamp10 software (Molecular Devices). For membrane capacitance and I_{Ca} measurement, the internal solution contained (in mM) 130 CsCl, 10 NaCl, 10 tetraethylammonium chloride (TEA-Cl), 5 EGTA, 3 magnesium ATP and 10 HEPES, pH 7.2. For membrane capacitance measurements, the external solution contained (in mM) 140 NaCl, 5 CsCl, 2 $CaCl_2$, 1 $MgCl_2$, 10 glucose and 10 mM HEPES, pH 7.2. To estimate cell size, bright-field images were taken before patch clamping through an Andor Clara DR-328G charge-coupled device (CCD) camera in a Nikon TE2000U microscope. ImageJ software was used to measure the cell size. For I_{Ca} recordings, the external solution contained (in mM) 140 TEA-Cl, 5 CsCl, 2 $CaCl_2$, 1 $MgCl_2$, 10 glucose and 10 HEPES, pH 7.2. To obtain the current-voltage relationship of I_{Ca}, test pulses were elicited from −90 to +50 mV with 10-mV increments. Both the holding and repolarizing potentials were −90 mV.

To measure the diffusion barrier inside the cardiomyocyte T tubules, I_{Ca} or I_{K1} was monitored while switching extracellular solutions with different calcium or potassium concentrations using a fast perfusion system (VC3-8xP pressured perfusion system, ALA Scientific Instruments). The protocol shown in **Figure 2a** was used to measure calcium diffusion. In brief, the I_{Ca} was elicited by four conditioning pulses followed by a test pulse. Both the conditioning and test pulses were from −80 to 0 mV for 200 ms. The delay between the conditioning pulses and the test pulse was gradually prolonged (with a stepwise 50-ms increment) during which the extracellular solution with 2 mM calcium was quickly switched to a solution with 5 mM EGTA. The change of I_{Ca} was normalized to the current of the fourth conditioning pulse (I_{max}) and fitted with one plateau followed by one phase of exponential decay. A dead time of 124 ms due to dead volume was subtracted before fitting.

The intracellular solution for measuring the inward rectifying potassium channel–mediated I_{K1} current contained (in mM) 100 potassium gluconate, 30 KCl, 1 $MgCl_2$, 1 EGTA, 3 sodium ATP, 10 glucose and 10 HEPES, pH 7.3. The extracellular solution contained (in mM) 5 or 8.1 KCl, 140 NaCl, 1.8 $CaCl_2$, 1 $MgCl_2$, 0.2 $CdCl_2$, 10 glucose and 10 HEPES, pH 7.3. The kinetics of the I_{K1} changes after a quick switch of extracellular potassium concentration from 5 to 8.1 mM were continuously recorded by holding the cardiomyocytes at −80 mV. The kinetics were fitted with one plateau followed by one phase of exponential decay. The dead time of the perfusion system between solution switches was 124 ms (measured by monitoring the changes of junction potential; data not shown) and was subtracted from the initial delay time shown in **Figure 3**.

All experiments were performed at room temperature (22–24 °C). Series resistance was compensated at 60–75% and monitored during the experiment. Recordings were filtered at 2–5 kHz and digitized at 10 kHz (Digidata 1440A, Molecular Devices). Clampfit 10 (Molecular Devices), Origin 7.5 (OriginLab) and Prism (Graphpad software) were used for data analysis.

Mathematical modeling of calcium diffusion in T tubules. A set of one-dimensional partial differential equations (PDEs) was developed to model calcium dynamics in the T tubule. There are three time-dependent variables: the calcium concentration in the rapid diffusion zone, $c_1(x,t)$; the number of calcium ions in the slow diffusion zone, $N_2(t)$; and the concentration of EGTA in the fast diffusion zone, $c_E(x,t)$ (**Fig. 2d**). In our model, the slow diffusion zone can only exchange with the rapid diffusion zone at the distal end of the T tubule farthest from the extracellular space. The equations are:

$$\frac{\partial c_1(x,t)}{\partial t} = \tau_{Ca} D_{Ca} \frac{\partial^2 c_1(x,t)}{\partial x^2} - \delta(x) \cdot k(c_1(x,t) - c_2(t)) - \sigma c_1 \cdot c_E$$

$$\frac{dN_2(t)}{dt} = k(c_1(0,t) - c_2(t))$$

$$\frac{\partial c_E(x,t)}{\partial t} = \tau_E D_E \frac{\partial^2 c_E(x,t)}{\partial x^2} - \sigma c_1 \cdot c_E$$

where k is the exchange rate between calcium in the slow and rapid diffusion zones, c_2 is the concentration of calcium in the slow diffusion zone ($c_2 = N_2/V_2$), σ is a rate constant for Ca^{2+} chelation by EGTA, D_{Ca}[55] and D_E[56] are the free diffusion constants of Ca^{2+} and EGTA, respectively, and τ_{Ca} and τ_E are tortuosity factors for Ca^{2+} and EGTA, respectively, that account for reduced diffusion in the T tubule. The delta function, $\delta(x)$, indicates that compartment exchange only influences c_1 at the $x = 0$ end of the T tubule.

The equations were solved in Matlab (2012a, The MathWorks, Natick, MA) using customized code. At each time step, the spatial diffusion terms for c_1 and c_E were first solved with a standard Crank-Nicholson tridiagonal scheme[57].

doi:10.1038/nm.3543

Next, $N_2(t)$, $c_1(0,t)$ and the chemical terms involving chelation, $\sigma c_i c_E$, were updated using a simple Euler method. The movement of ions across the boundary between slow and rapid zones involves geometric factors to properly convert the change in ion numbers in the slow diffusion space, ΔN_2, to a change in concentration in the rapid diffusion zone, Δc_1. Division of ΔN_2 by V_1, the volume of the first spatially discretized element in the rapid diffusion zone, properly converts moles to concentration. V_1 is the cross-sectional area of the rapid diffusion zone of the T tubule, A, times the spatial discretization along the length of the tubule, dx, such that $V_1 = A\mathrm{d}x$. Initially, the calcium concentration was assumed to be uniform at 2 mM in both compartments, but the value was set to zero at the far right boundary, x = L (the T-tubule length), which corresponds to the bulk extracellular space. The right boundary was therefore treated as a Dirichlet boundary condition. The calcium concentration at the inner boundary, $x = 0$, was treated with a Neuman-type reflecting boundary condition. The EGTA concentration was initially set to zero in the rapid diffusion zone except where it was fixed to 2 mM at x = L. c_E was also treated with reflecting boundary conditions at $x = 0$ in the same manner as c_1. The convergence properties of the solution were investigated, and the discretization values shown in **Supplementary Table 1** for dt and dx provide well converged solutions.

The mathematical model was fit to the WT data in **Figure 2e** using a Nelder-Mead Simplex method[57] provided in the Matlab package NMSMAX.m[58]. The six parameters indicated in **Supplementary Table 1** were systematically varied, and the closeness of the modeled curve to the experimental data was calculated using the following error function:

$$Error = -\sum_{i=1}^{N} \left| Y_i - Y_i^* \right|$$

where i runs over all experimental data points, Y_i is the experimental value of the normalized current for point i, and Y_i^* is the normalized calcium concentration in the slow diffusion zone corresponding to the time of point i. The search algorithm was run in 10–20 iterative rounds using the best fit from one round as the initial condition for further runs. Each round was run for 200–1,000 iterations. After fitting the model to the WT data, the diffusion barrier between compartments was removed by increasing the value of k by a factor of 100, and the normalized concentration in the slow diffusion zone was replotted without further fitting of the data. All code will be provided upon request to M.G. (michael.grabe@ucsf.edu).

Optical mapping. Optical mapping was performed on mouse hearts, which were rapidly harvested after anesthesia and arrested in cold cardioplegia solution. The aorta was cannulated and retrogradely perfused with 37 °C modified Tyrode solution ((in mmol l^{-1}) NaCl 120, $NaHCO_3$ 18, KH_2PO_4 1.2, $MgSO_4$ 1.2, glucose 11, $CaCl_2$ 1.8, sodium pyruvate 5, mannitol 1 and KCl 3.8) bubbled with 95% O_2 and 5% CO_2. Hearts were then placed in a temperature-controlled optical recording chamber (maintained at 37 °C) while electrocardiograms and perfusion pressures were measured continuously. Before optical recording, Tyrode solution containing the voltage-sensitive dye Di-4-ANEPPS (10 µl of 2.5 mM stock) was perfused through the hearts. Contractility was blocked using 5 µM blebbistatin (Sigma). For studies of low and high extracellular K^+ perfusion, the KCl concentration in Tyrode solution was adjusted to achieve a total K^+ concentration of 2.5 (low) or 8 (high) mM, as compared to the standard 5 mM K^+ concentration in the normal Tyrode solution.

The optical mapping system used has been previously described[59]. Briefly, action potentials were simultaneously recorded at 1,000 Hz with a 100 × 100 complementary metal oxide semiconductor (CMOS) camera with a 10 × 10 mm mapping field on the epicardium of the left ventricle anterior wall. Fluorescence was excited using a 1,000-W tungsten-halogen light source with a filter of 530 nm and transmitted with an emission long-pass filter of 630 nm. Pacing was performed from two sites sutured with silver electrodes: first with one on the apex of the left ventricle with pacing cycle lengths (PCLs) from 150 to 70 ms and then with S1–S2 using a basic PCL of 150 ms and S2 decremented by 2 ms until the ventricular effective refractory period was reached. After this, a train of programmed stimulation with up to three extra stimuli after a basic PCL of 150 ms (S1–S4 stimulation protocol) and a burst pacing from 60 to 30 ms (decrement by 2 ms) were performed to induce ventricular arrhythmias. The other site is on the left atrium paced with simulated heart rates of 300, 400, 600 and 800 beats per min in order to induce ectopic ventricular beats.

Data analysis was performed using custom Matlab (MathWorks, Natick, MA) programs designed for the analysis of optically recorded action potentials. Quantitative data were obtained from optically derived action potentials for each of the 10,000 pixels of the CMOS camera. Local activation was determined as the time point of maximum change in fluorescence over time (dF dt^{-1}) for each fluorescent signal in the array. Isochronal activation maps and conduction velocity were analyzed as described previously[60]. The action-potential duration (APD) at 80% repolarization (APD_{80}) was determined as the time difference between the takeoff potential and the point during repolarization at 20% of the maximal action-potential amplitude.

***In vivo* cardiac electrophysiology studies in adult mice.** Invasive intracardiac electrophysiology was studied in young adult mice (8 weeks old) following a previously established protocol with some modifications[33]. Mice were anesthetized with 1% isoflurane in 100% oxygen, body temperature was maintained at 37 °C with a heating pad, and respiration was maintained using a respirator connected to an endotracheal tube placed into the mouse trachea. EKGs were recorded using PowerLab (ADInstruments) during the whole experimental procedure. After lateral thoracotomy, the heart was visualized, and two platinum electrodes were placed on the apex of the left ventricle for pacing. A constant current stimulus isolator (FE180, ADInstruments, Colorado Springs, CO) was used to deliver pacing currents, which was interfaced with a software-driven programmed electrical stimulator (LabChart Pro, ADInstruments, Colorado Springs, CO). Pacing thresholds were then determined, and stimulation was delivered at a 0.3- to 0.4-ms pulse width at twice the capture threshold. Standard triple extrastimulations were performed. A drive cycle length of 80 ms (S1) was followed by S2 decremented by 2 ms until the ventricular effective refractory period was reached. After this, a train of programmed stimulation with three extra stimuli after S1 (S1–S4) was performed and repeated every 10 s for 10 min to determine the incidence and frequency of induced VT. After baseline experiments, isoproterenol (0.1 mg kg^{-1} body weight) was injected into left ventricle, and 10 min were allowed to elapse for stabilization of heart rate before the same S1–S4 pacing protocol was repeated. Nonsustained VT was defined as four to nine consecutive beats, and sustained VT was defined as >9 QRS complexes not preceded by superventricular activity[32]. LabChart was used for data analysis.

***In vitro* actin complex formation using heart lysates.** Adult mouse hearts were perfused through the aorta to remove blood and lysed in actin polymerization buffer ((in mM) 150 KCl, 20 HEPES, 2 $MgCl_2$, 2 K_2HPO_4 and 1% NP-40, pH 7.4, with halt protease inhibitor). After a 10-min incubation on ice, the lysate was ultracentrifuged for 1 h at 170,000g at 4 °C in a benchtop Beckman type Ti-50 fixed-angle rotor to remove endogenous F-actin polymers. The F-actin–free supernatant was collected and divided equally into four aliquots. Each of the aliquots was then supplemented with various GST-BIN1 isoform–coated glutathione beads (BIN1, BIN1+13, BIN1+17 and BIN1+13+17), which were prepared fresh by incubating glutathione beads with lysates of FT293 cells overexpressing different GST-BIN1 isoforms (2 h incubation at 4 °C). The F-actin–free heart lysates supplemented with BIN1 beads were then rotated head to toe overnight (16 h) at 4 °C in the presence of 25 µM phallodin and 100 µM ATP, allowing for *in vitro* actin polymerization. Then the BIN1-coated beads were spun down and washed three times in actin polymerization buffer at 4 °C. BIN1 and its associated protein complex were eluted from the beads in SDS-PAGE sample buffer (70 °C for 10 min) and resolved by gel electrophoresis.

GST-BIN1 pulldown experiments. For GST-BIN1–mediated pulldown of α-actinin, adult hearts were lysed in 0.5% NP-40 buffer ((in mM) 150 KCl, 20 HEPES, 2 $MgCl_2$, 2 K_2HPO_4, 1 dithiothreitol (DTT), 1 NaF, 0.1 Na_3VO_4 and 0.5% NP-40, pH 7.4, with halt protease inhibitor). The lysates were then divided equally into four portions and incubated with purified GST-BIN1–, GST-BIN1+13–, GST-BIN1+17– or GST-BIN1+13+17–coated glutathione beads prepared as described in the previous section. The lysates were rotated head to toe at 4 °C for 2 h to allow for protein complex formation. BIN1 protein complex–attached beads were then washed and eluted in SDS-PAGE (NuPage LDS) sample buffer (Life Technologies) (70 °C for 10 min). The eluted samples

were resolved by western blot analysis for the detection of α-actinin (rabbit anti–α-actinin, Abcam, ab72592) and GST-BIN1 (rabbit anti-GST, Santa Cruz Biotechnology, sc-459).

For BIN1 pulldown of N-WASP, HeLa cells overexpressing N-WASP–V5 and GST-BIN1 protein isoforms were lysed and incubated with glutathione beads at 4 °C for 30 min. The proteins were then separated by electrophoresis followed by western blot analysis. Rabbit anti-V5 (Sigma, 1:3,000) and rabbit anti-GST (Santa Cruz Biotechnology, 1:1,000) antibodies were used as primary antibodies.

***In vitro* actin polymerization assay.** The Actin Polymerization Biochem Kit, purified Arp2/3 protein complex and purified VCA domain of N-WASP were obtained from Cytoskeleton. GST-fused N-WASP and BIN1 protein isoforms were purified by glutathione bead pulldown followed by elution with 5 mM glutathione. Protein was then concentrated and washed with Amicon concentrator to reach a final concentration of 10 μM in 100 mM Tris (pH 7.4) buffer, in order to be compatible with the actin assay. The manufacturer's actin polymerization protocol was optimized using 0.2 mg ml^{-1} 100% pyrene-labeled actin (Cytoskeleton) supplemented with 60 nM Arp2/3 protein complex and N-WASP (200 nM) in the presence of control GST-GFP protein or 1 μM of BIN1 isoforms. Pyrene-actin alone (supplemented with GST-GFP for a similar total protein concentration) was used as the negative control. For the positive control, N-WASP was replaced with 200 nM purified N-WASP VCA domain. Baseline pyrene fluorescence (excitation at 360 nm and emission at 410 nm) and 90-min polymerization kinetics were recorded with a FlexStation 3 Microplate Reader (Molecular Devices). SoftMax Pro 5.4.5 (Molecular Device) was used for data analysis, including V_{max} calculation.

Signal processing and statistical analyses. Fluorescence intensity profiles were generated by ImageJ. Prism 5 (GraphPad) software was used for statistical analyses. For comparison between two groups, a paired or unpaired two-tail Student's *t* test was performed. For comparison among three or more treatment groups, one-way ANOVA followed by Dunnet's post test was performed. For I_{Ca} and I_{K1} decay kinetics, the curves were fit with one-plateau followed by one-phase exponential decay in Prism. For comparison of VT incidence among three genetic groups, the χ^2 test was used, and for comparison of VT frequency before and after isoproterenol among three genetic groups, two-way ANOVA was used.

48. Smyth, J.W. *et al.* Actin cytoskeleton rest stops regulate anterograde traffic of connexin 43 vesicles to the plasma membrane. *Circ. Res.* **110**, 978–989 (2012).
49. O'Connell, T.D., Rodrigo, M.C. & Simpson, P.C. Isolation and culture of adult mouse cardiac myocytes. *Methods Mol. Biol.* **357**, 271–296 (2007).
50. Hattori, F. *et al.* Nongenetic method for purifying stem cell–derived cardiomyocytes. *Nat. Methods* **7**, 61–66 (2010).
51. Leach, R.N., Desai, J.C. & Orchard, C.H. Effect of cytoskeleton disruptors on L-type Ca channel distribution in rat ventricular myocytes. *Cell Calcium* **38**, 515–526 (2005).
52. Novak, P. *et al.* Nanoscale live-cell imaging using hopping probe ion conductance microscopy. *Nat. Methods* **6**, 279–281 (2009).
53. Kremer, J.R., Mastronarde, D.N. & McIntosh, J.R. Computer visualization of three-dimensional image data using IMOD. *J. Struct. Biol.* **116**, 71–76 (1996).
54. Mastronarde, D.N. Dual-axis tomography: an approach with alignment methods that preserve resolution. *J. Struct. Biol.* **120**, 343–352 (1997).
55. Shorten, P.R. & Soboleva, T.K. Anomalous ion diffusion within skeletal muscle transverse tubule networks. *Theor. Biol. Med. Model.* **4**, 18 (2007).
56. Kits, K.S., de Vlieger, T.A., Kooi, B.W. & Mansvelder, H.D. Diffusion barriers limit the effect of mobile calcium buffers on exocytosis of large dense cored vesicles. *Biophys. J.* **76**, 1693–1705 (1999).
57. Press, W. *Numerical Recipes: The Art of Scientific Computing* (Cambridge University Press, 2007).
58. Higham, N.J. Optimization by direct search in matrix computations. *SIAM J. Matrix Anal. Appl.* **14**, 317–333 (1993).
59. Nguyen, D.T., Ding, C., Wilson, E., Marcus, G.M. & Olgin, J.E. Pirfenidone mitigates left ventricular fibrosis and dysfunction after myocardial infarction and reduces arrhythmias. *Heart Rhythm* **7**, 1438–1445 (2010).
60. Salama, G., Kanai, A. & Efimov, I.R. Subthreshold stimulation of Purkinje fibers interrupts ventricular tachycardia in intact hearts. Experimental study with voltage-sensitive dyes and imaging techniques. *Circ. Res.* **74**, 604–619 (1994).

doi:10.1038/nm.3543